Komatsu *et al. Earth, Planets and Space* (2017) 69:101
DOI 10.1186/s40623-017-0683-6

Earth, Planets and Space

LETTER

Open Access

Three-dimensional P- and S-wave attenuation structures around the source region of the 2016 Kumamoto earthquakes

Masanao Komatsu*, Hiroshi Takenaka and Hitoshi Oda

Abstract

We investigate the three-dimensional P- and S-wave attenuation (Q_P^{-1} and Q_S^{-1}) structures of the crust around the source region of the 2016 Kumamoto earthquakes, Japan. To estimate the attenuation structures, the path-averaged attenuation factor t^* is estimated from the amplitude decay rate of the P- and S-wave spectra corrected for the source spectrum. The Q_P^{-1} and Q_S^{-1} structures are estimated by tomography using t^* for the P- and S-waves, respectively. Several features are found in the attenuation structures as follows: In the source region, two high-Q_P and high-Q_S zones exist along the Futagawa and the Hinagu fault segments in the upper crust. The high-Q_P and high-Q_S zone along the Futagawa fault segment is found to include the large-slip area of the mainshock obtained from a source inversion study. In the lower crust, the low Q_P is distributed beneath the entire source region. A low-Q_P and low-Q_S zone also exists beneath the Kuju and Aso volcanoes, which is consistent with the shallow limited depth extent of the seismogenic zone due to high temperature. The western edge of this zone adjoins the eastern edge of the high-Q_P and high-Q_S area, including the large-slip area.

Keywords: 2016 Kumamoto earthquakes, Attenuation structure, Seismicity, Active volcano

Introduction

Two large events during the 2016 Kumamoto earthquakes caused a great deal of damage in Kumamoto and Oita Prefectures, Kyushu Island, Japan. The largest foreshock (M_{JMA}6.5; indicated by the green star in Fig. 1a) occurred at 21:26 on April 14, 2016 (JST: UTC + 9 h), and then, the mainshock (M_{JMA}7.3; indicated by the yellow star in Fig. 1a) took place at 01:25 on April 16, 2016 (JST). The epicenter of the mainshock was located near the intersection of the Futagawa and Hinagu faults, which are reported to be active faults (Nakata and Imaizumi 2002). During the mainshock, a moderate event (M_{JMA}5.7; indicated by the sky blue star in Fig. 1a) was induced near the Yufu-dake volcano, Oita Prefecture (e.g., Yoshida 2016). After the mainshock and the induced event, the aftershock activity extended toward the NE, where the active volcanoes, Mt. Aso, Mt. Kuju, Mt. Yufu-dake, and Mt. Tsurumi-dake, are located (Fig. 1a).

Kyushu Island is located in southwest Japan. The Philippine Sea (PHS) plate is subducting beneath this region along the Nankai Trough. The active volcanoes mentioned above are located along the volcanic front on Kyushu Island. The sequence of the 2016 Kumamoto earthquakes and the induced event occurred through this volcanic area in the central Kyushu Island, across which the Beppu–Shimabara graben lies oriented NE–SW. Along the graben, a shear zone (western extension of the median tectonic line) is present under the north–south extensional stress regime where both normal faulting and strike-slip earthquakes have occurred (Matsumoto et al. 2015). The Futagawa and Hinagu faults are in the southwestern portion of the shear zone.

The quality factor Q expresses the degree of anelasticity of rocks and depends on the temperature and water content (e.g., Karato 2003). Generally, P- and S-wave Q (Q_P and Q_S) show that the condition $Q_S > Q_P$ is found in the crust (e.g., Rautian et al. 1978; Modiano and Hatzfeld

*Correspondence: pcb58mxh@s.okayama-u.ac.jp
Graduate School of Natural Science and Technology, Okayama University, Tsushima-Naka 3-1-1, Okayama 700-8530, Japan

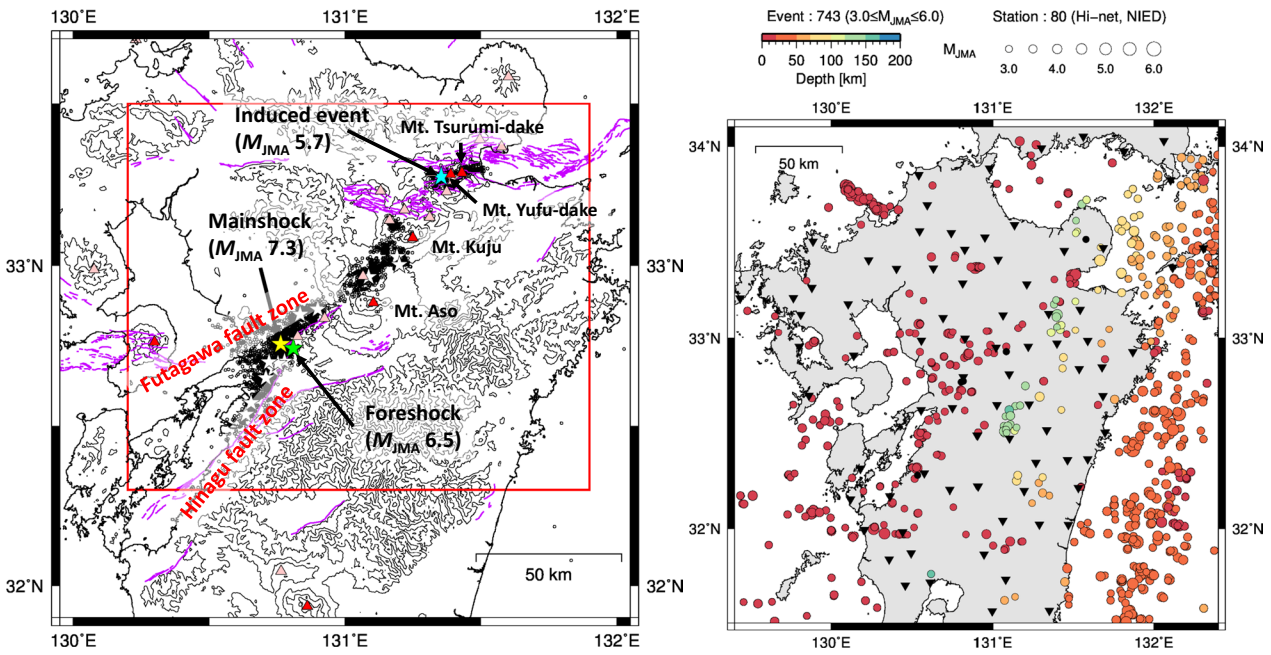

Fig. 1 **a** Tectonic background and **b** events and stations used in this study. *Green*, *yellow*, and *sky blue stars* indicate the epicenters of the largest foreshock (M_{JMA}6.5), the mainshock (M_{JMA}7.3), and the induced event (M_{JMA}5.7), respectively. *White stars* denote the epicenters of events larger than M_{JMA} 5.0 for one month following the foreshock. *Black circles* indicate the epicenters of events with $2.0 \leq M_{JMA} < 5.0$ occurring for one month following the foreshock. Active and quaternary volcanoes are shown as *red* and *peach triangles*, respectively. *Purple lines* denote active faults (Nakata and Imaizumi 2002). *Black lines* are contours of altitude with intervals of 300 m. The *red square* corresponds to the area shown in Fig. 2. *Colored circles* and *inverse triangles* show the events and stations used in this study. The *color* and *size of each circle* indicate the depth and the magnitude of the event, respectively

1982), whereas the condition $Q_P > Q_S$ dominates in the asthenosphere (e.g., Anderson et al. 1965). Several three-dimensional Q tomographic studies have been conducted for southwestern Japan, including Kyushu Island (Liu and Zhao 2014, 2015; Saita et al. 2015; Komatsu and Oda 2015). These results revealed the low-Q zones upwelling from the top of the high-Q PHS slab to the active volcanoes. Liu and Zhao (2015) showed that low-Q zones in the crust are located in or around the active faults. They interpreted that large crustal earthquakes might be caused by fluids due to dehydration on the PHS slab. Mamada and Takenaka (2004) investigated the Q_S structure around the source region of the 1997 Northwestern Kagoshima earthquakes in southern Kyushu with the coda normalization method and found that the focal region of these earthquakes have lower Q than outside of the focal region. Most recently, Wang et al. (2017) estimated the 3-D attenuation and velocity structures in the source region of the 2016 Kumamoto earthquakes from the data including events before and after these earthquakes and found that the Kumamoto earthquakes occurred in a high-Q and high-velocity zone in the upper crust underlain by a low-Q, low-velocity, and high-Poisson's ratio area in the lower crust and upper mantle.

Komatsu and Oda (2015), our previous study, estimated the 3-D P-wave attenuation structure beneath southwest Japan, including Kyushu. The obtained tomographic image illustrates that a low-Q_P zone exists around the Beppu–Shimabara graben and active volcanoes, while a high-Q_P zone exists in the PHS slab. In this study, we estimate the Q_P and Q_S structures beneath the source region of the 2016 Kumamoto earthquakes and discuss the relationship among Q_P, Q_S, and geophysical phenomena (fluid content, thermal structure, seismicity, and rupture process).

Data and methods

The study area is the central part of Kyushu Island, which is situated at 31.5°N–34.1°N and 129.4°E–132.4°E (Fig. 1b). We use seismograms recorded by 80 stations within the High Sensitivity Seismograph Network Japan (Hi-net) deployed by the National Research Institute for Earth and Disaster Resilience (NIED) (Okada et al. 2004). We select 743 crustal and intra-slab events (M_{JMA} 3.0–6.0) occurring in and around Kyushu Island in the period from June 2002 to May 2012 (Fig. 1b). Note that

the period is before the Kumamoto earthquakes took place. These events were also used in the study of the three-dimensional P-wave attenuation structure beneath southwest Japan (Komatsu and Oda 2015).

We first determine the path-averaged attenuation factor t^* from the waveform data through a spectral analysis. The seismic displacement spectra of P- and S-waves for event i observed at station j may be expressed as

$$U_{ij}(f) = \Omega_{0i} S_i(f) \cdot \exp\left(-\pi f t_{ij}^*\right), \tag{1}$$

$$S_i(f) = \frac{1}{1 + \left(\frac{f}{f_{ci}}\right)^2}, \tag{2}$$

where f is the frequency, Ω_{0i} is a frequency-independent term related to the seismic moment, and f_{ci} is the corner frequency of the source spectrum $S_i(f)$ (Scherbaum 1990; Eberhart-Phillips and Chadwick 2002). The attenuation factor t_{ij}^* contains information on Q along the ray path from the hypocenter i to station j. In order to determine t_{ij}^*, Eq. (1) is rewritten as

$$\log\left|U_{ij}(f)/S_i(f)\right| = \left(-\pi t_{ij}^* \log e\right) f + \log \Omega_{0i}. \tag{3}$$

Since there is a trade-off between the f_{ci} included in $S_i(f)$ and t_{ij}^* (e.g., Scherbaum 1990; Ko et al. 2012), before evaluating t_{ij}^*, we independently estimate f_{ci} using a procedure exploited by Somei et al. (2014), which is based on the S-wave coda spectral ratio method (e.g., Aki and Chouet 1975) (see Additional file 1: Section 1 and Figure S1 for the description and example of the f_c estimation).

In evaluating t^* based on Eq. (3), the original velocity records are transformed into the displacement records, and the displacement spectra are estimated from the signals in a window of 3 s duration, beginning 0.5 s before the P- or S-wave arrivals. The P-wave spectrum is calculated from the vertical component seismogram, while the S-wave spectrum is obtained by the square root of the sum of the squared NS and EW spectral amplitudes of the S-wave. Here, Ω_{0i} and t_{ij}^* are determined for the frequency range of 3–30 Hz by fitting Eq. (3) to the observed spectrum, where we used the P- and S-wave corner frequencies estimated by Komatsu and Oda (2015) (see Additional file 1: Fig. S2 for examples of the waveforms and spectra). Consequently, 11512 P-wave t^* and 11820 S-wave t^* data were obtained.

The attenuation factor t^* for the P- or S-wave propagating into a three-dimensionally heterogeneous structure may be represented as

$$t^* = \int_{\text{ray path}} \frac{\mathrm{d}s}{v_{(x,y,z)} Q_{(x,y,z)}}, \tag{4}$$

where v is the seismic velocity (Thurber 1983), and the integration is performed along a ray path between the event and the station. When a three-dimensional grid is placed in the target space, Eq. (4) is discretized into a linear equation of Q^{-1} at the grid nodes in the vicinity of the ray path (Thurber 1983; Komatsu and Oda 2015). Since a set of the linear equations is obtained for all event–station pairs, we can conduct Q tomography from the t^* data by solving it for Q^{-1} of the grid nodes. The grid intervals are set to be 0.125° in the lateral directions and 5–50 km along the depth direction. These intervals are smaller than those used by Liu and Zhao (2014, 2015), Saita et al. (2015), Komatsu and Oda (2015), and Wang et al. (2017). For calculation of the ray paths of the P- and S-waves, we employ a 1-D velocity structure, which is based on the JMA2001 model (Ueno et al. 2002). The crustal velocity structure consists of two homogeneous layers ($V_P = 6.02$ km/s and $V_S = 3.53$ km/s for the upper crust; $V_P = 6.70$ km/s and $V_S = 3.89$ km/s for the lower crust), each of which is 15 km in thickness. The P- and S-wave ray paths and travel times are calculated with a ray tracing technique developed by Zhao et al. (1992, 1994). We use a nonnegative least squares method (Lawson and Hanson, 1974) for the t^* inversion to obtain the Q^{-1} structures for the P- and S-waves, so that the Q^{-1} values estimated at grid nodes are always positive.

Results

To see how correctly the Q_P and Q_S structures are restored by inversion of the t^* data, we perform checkerboard resolution tests (CRTs) (e.g., Zhao et al. 1992) using synthetic t^* data produced from a structure where $Q^{-1} = 0.001$ and 0.007 (Kita et al. 2014) are alternately assigned to the size of 0.25° [longitude] × 0.25° [latitude] × 10–75 km [depth direction] at depths of 2–250 km. The synthetic t^* values are calculated along the same ray paths as those of the real analysis of the observed t^* data. Random noise with a standard deviation of 0.001 s is then added to the synthetic t^*. The Q^{-1} values at grid nodes are determined by inversion of the synthetic t^* data using the same velocity structure as the actual tomography (Additional file 1: Figure S3). After inverting this dataset, we examine the results of the CRTs by resolvability R (Zelt 1998; Saiga et al. 2010) (see Additional file 1: Section 2). When the resolvability R of Q^{-1} value recovered at each grid is larger than 0.75, the Q^{-1} structure is judged to be restored with high resolution (Saiga et al. 2010). We also carry out another set of restoring resolution tests (RRTs) (e.g., Zhao et al. 1992). The RRTs are similar to the CRTs, except for the input model that is constructed from the obtained Q^{-1} structure (Additional file 1: Figure S4). The results for the CRTs and the RRTs illustrate that the structures are well

restored down to 20 km (Additional file 1: Figures S3 and S4).

Figure 2 shows the lateral variation of Q_P and Q_S at 7, 12, and 17 km depths in the crust. The area shaded by gray indicates a low resolution region, where resolvability R is smaller than 0.75 in the CRTs (Additional file 1: Figure S3). In the source region of the 2016 Kumamoto earthquakes (area of 130.5°E–131°E and 32.5°N–33°N), high-Q_P and high-Q_S areas exist at 7 and 12 km depths, where large aftershocks (white stars) occurred. There also

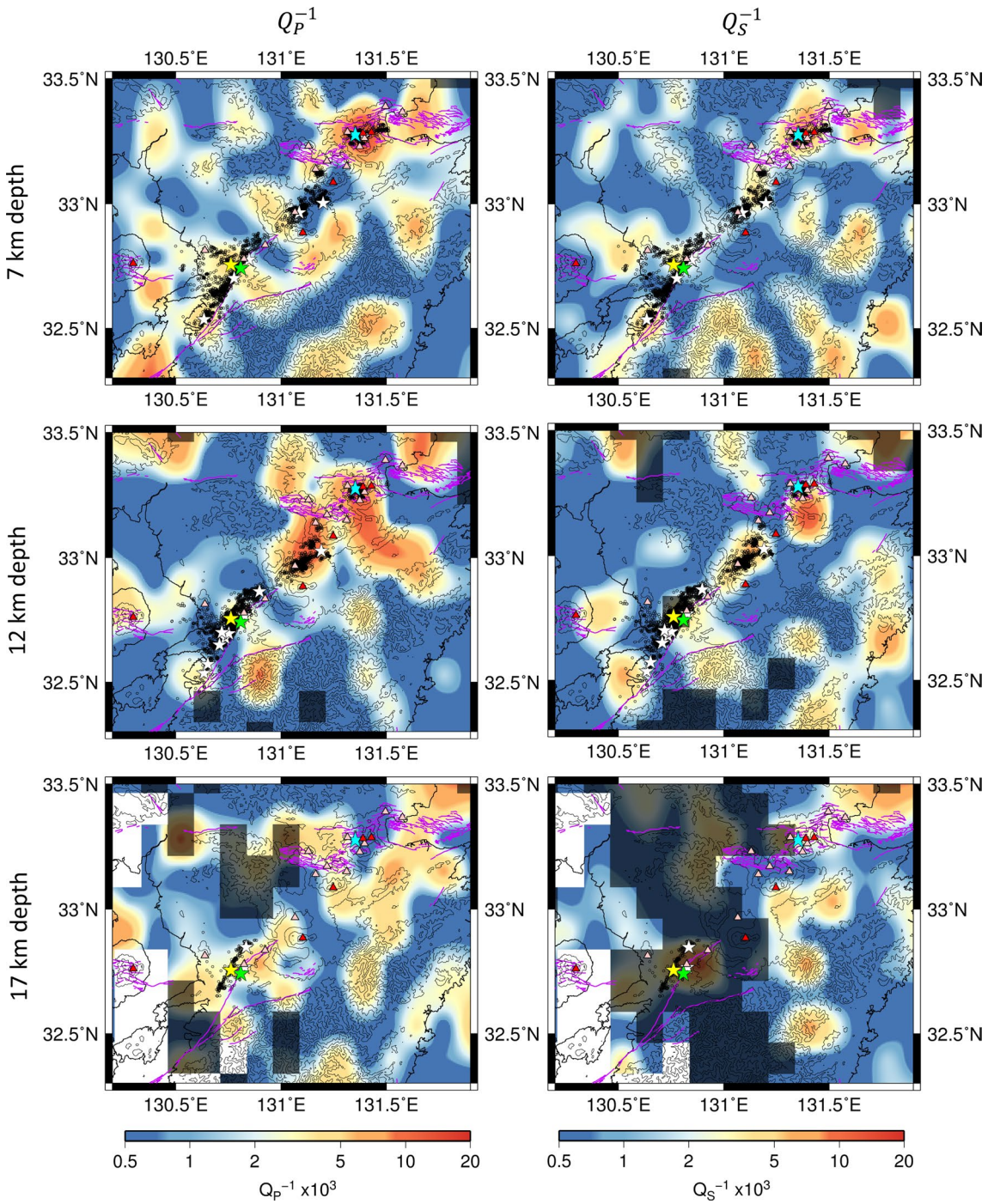

Fig. 2 Lateral distribution of estimated Q_P^{-1} and Q_S^{-1} in the crust. The region *shaded by gray* shows low resolution, where the resolvability R is smaller than 0.75. See the caption of Fig. 1 for explanation of the *lines* and *symbols*

exists a localized low-Q_P patch in which the epicenters of the largest foreshock (green star) and mainshock (yellow star) are located. In the lower crust, a low-Q_P zone is distributed beneath the source region. Beneath the active volcanoes (Mt. Aso, Mt. Kuju, Mt. Yufu-dake, and Mt. Tsurumi-dake indicated by the red triangles in the range 131°E–131.5°E), the low-Q_P and low-Q_S zone extends toward the lower crust (Fig. 2 and Additional file 1: Figure S5).

For comparing Q_P with Q_S in the crust, we also estimate the Q_P/Q_S structure directly using the S-wave t^* data and the estimated Q_P^{-1} structure (Pozgay et al. 2009). In the estimation of Q_P/Q_S, for Q_P^{-1} smaller than 0.0005, we assume $Q_P^{-1} = 0.0005$. The resolution of Q_P/Q_S is evaluated from both the CRTs for Q_P and Q_S. This result shows that, in the crust, Q_S is basically larger than Q_P (Additional file 1: Figure S6). This trend is consistent with the relationship between Q_P and Q_S reported in previous studies (e.g., Rautian et al. 1978; Modiano and Hatzfeld 1982).

Figure 3 displays Q_P and Q_S structures on the vertical cross sections along three lines: line A–B (from Mt. Yufu-dake to Mt. Aso), line B–C (along the Futagawa fault), and line C–D (along the Hinagu fault). Low-Q_P and low-Q_S zones exist beneath Mt. Yufu-dake (in depth of 5–15 km along line A–B) and between Mt. Kuju and Mt. Aso (in depth of 10–15 km along line A–B) and reach a depth of 25 km beneath Mt. Kuju (line A–B). In these low-Q_P and low-Q_S areas, the lower limit of the seismicity is shallower than that in the source region along lines B–C and C–D. Many aftershocks occurred between the high- and low-Q_P patches beneath the area from Mt. Kuju to Mt. Aso, while beneath Mt. Yufu-dake, aftershocks locally took place in a low-Q_P and low-Q_S zone. In the source region, two high-Q_P and high-Q_S zones are located in the upper crust, where many aftershocks occurred. Low-Q_P patches, where aftershock activity is lower than that in the source region, also exist in both edges of the high-Q_P zones.

Discussion

The Q_P and Q_S structures in the upper crust are different between the volcanic region along line A–B and the source region along lines B–C and C–D (see Fig. 3). In the volcanic region, low-Q_P and low-Q_S zones are distributed beneath active volcanoes, where the lower limit of seismicity is shallower than that in the source region as mentioned in the previous section (Fig. 3). Matsumoto et al. (2016) estimated the D_{95} depth distribution in Kyushu, which indicates the bottom depth of the

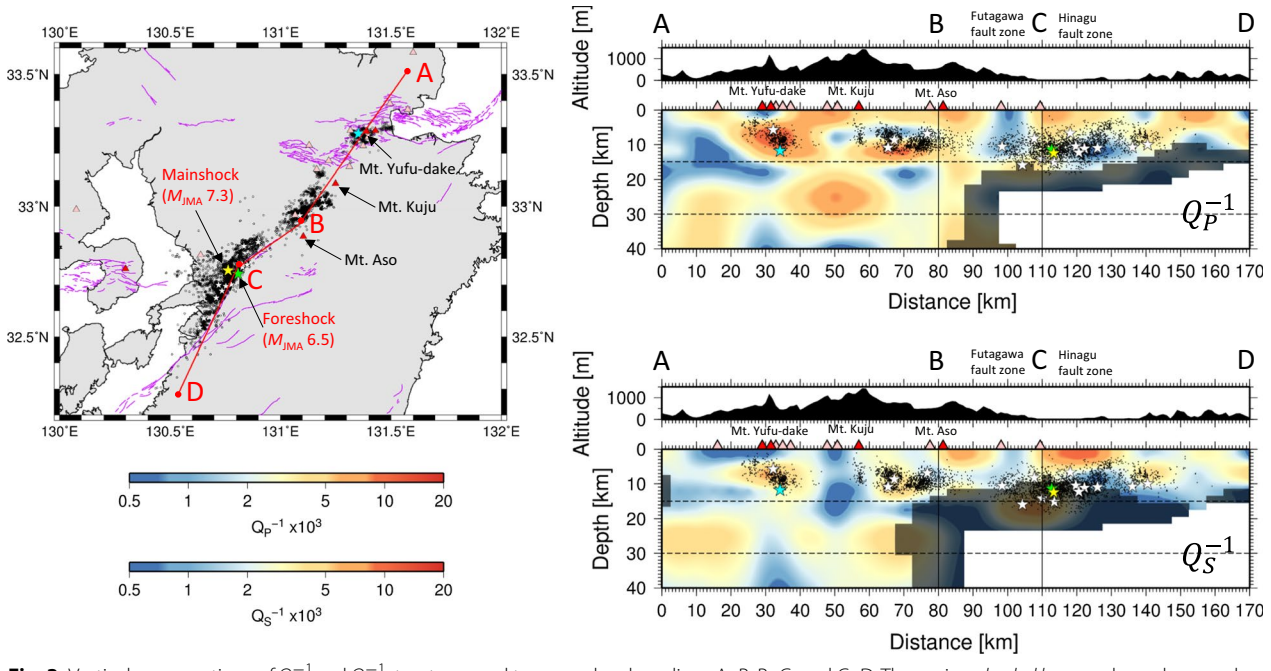

Fig. 3 Vertical cross sections of Q_P^{-1} and Q_S^{-1} structures and topography along lines A–B, B–C, and C–D. The region *shaded by gray* shows low resolution, where the resolvability R of the CRTs is smaller than 0.75. The Conrad and Moho discontinuities in the model are drawn by *dashed lines*. *Green*, *yellow*, and *sky blue stars* indicate the hypocenters of the largest foreshock (M_{JMA}6.5), the mainshock (M_{JMA}7.3), and the induced event (M_{JMA}5.7), respectively. *White stars* denote the hypocenters of events larger than M_{JMA}5.0 for 1 month following the foreshock. *Black dots* indicate the events with $2.0 \leq M_{JMA} < 5.0$ occurring for 1 month following the foreshock. See the caption of Fig. 1 for explanation of the *triangle symbols*

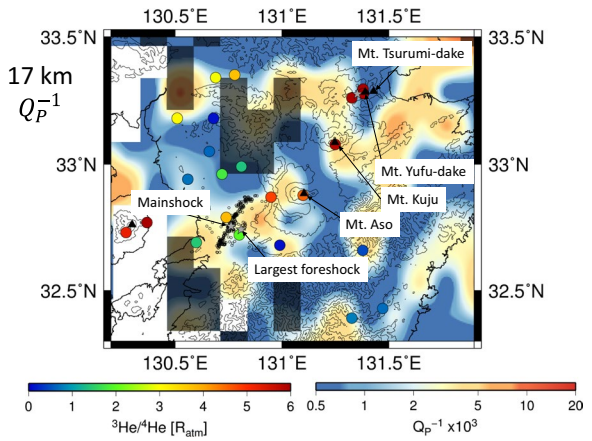

Fig. 4 Ratio of ^{3}He/^{4}He observed by Horiguchi and Matsuda (2013), which is plotted on the estimated Q_P structure at 17 km depth shown in Fig. 2. *Circles* are *color coded* according to ^{3}He/^{4}He ratios in R_{atm}. *Gray stars* indicate the largest foreshock, mainshock, and induced event. The *small circles* are the epicenters of the aftershocks. The *black triangles* denote the active volcanoes

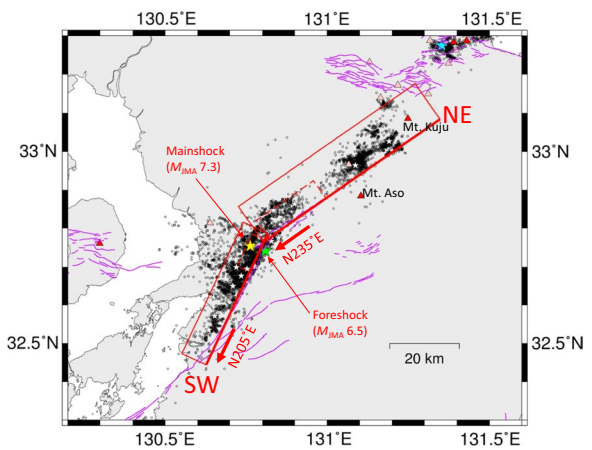

Fig. 5 Map of the Futagawa and Hinagu fault planes. The *solid red rectangles* show the areas of the planes used in Fig. 6 projected onto the surface, and the *red dashed rectangles* indicate the source fault planes of the mainshock and foreshocks estimated by Kato et al. (2016) and GSI (2016). Active faults (Nakata and Imaizumi 2002) are plotted by the *purple lines*. *Black circles* denote the events ($M_{JMA} \geq 2.0$) that occurred for 1 month following the foreshock. See the caption of Fig. 1 for explanation of the *star* and *triangle symbols*

seismogenic layer. The D_{95} depth in the volcanic region is shallower than that in the source region. Cho and Kuwahara (2013) estimated the thermal structure at the bottom of the seismogenic layer and revealed the existence of higher temperature in the volcanic region. The shallowing of the seismogenic zone around volcanoes might be due to weakening associated with the presence of magma.

In the source region, high-Q_P and high-Q_S zones are distributed in the upper crust except near the epicenters of the largest foreshock and mainshock (Fig. 2). Near the epicenters, a localized low Q_P exists. In the lower crust, a low-Q_P area is widely distributed below the source area. Most recently, Wang et al. (2017) also estimated the 3-D attenuation structure in the source region of the 2016 Kumamoto earthquakes and illustrated that the source region of the Kumamoto earthquakes is covered with a high-Q zone in the upper crust underlain by a low-Q zone in the lower crust, which is similar to the present study. Horiguchi and Matsuda (2013) investigated the ^{3}He/^{4}He ratio in water from various hot springs in central Kyushu. In Fig. 4, we plot their measured ^{3}He/^{4}He on the lateral variation of Q_P at 17 km depth in the lower crust. It is found that a high-^{3}He/^{4}He point exists close to the epicenter of the mainshock. Since the ^{3}He-rich fluids in the lower crust are thought to come from the upper mantle, the high ^{3}He/^{4}He ratio could be evidence of the high fluid content in the crust. In addition, Aizawa et al. (2017) estimated the resistivity structure in central Kyushu and showed that a high conductivity anomaly in the lower crust is distributed below the NW parts of the Futagawa and Hinagu faults. This indicates that the lower crust below the source region includes fluids from the upper mantle. The localized low-Q_P zone near the mainshock epicenter in the upper crust might be associated with the effect of fluids injected from the lower crust to the faults where the fault friction could be reduced.

To discuss the details of the variation of the Q_P and Q_S around the source region, we show the Q_P and Q_S structures along the source fault planes estimated by Kato et al. (2016) and the Geospatial Information Authority of Japan (2016) (GSI). Figure 5 shows a surface projection of the two fault planes, of which the strike and dip angles are N 235°E and 60° for the Futagawa fault, and N 205°E and 72° for the Hinagu fault, respectively. Figure 6 displays the Q_P and Q_S structures along the planes shown in Fig. 5. The two areas enclosed by the black dashed lines are the Futagawa and Hinagu segments of the fault source. The localized low-Q_P patch, including the hypocenters of the largest foreshock and mainshock, is put between two high-Q_P and high-Q_S patches (along strike, 0–20 km in the Futagawa segment and 5–25 km in the Hinagu segment). As mentioned above, a high ^{3}He/^{4}He ratio is observed close to the mainshock epicenter. This suggests that around the mainshock epicenter, fluids in the lower crust might enter faults in the upper crust, i.e., the seismogenic layer, and reduce the friction of the faults to trigger earthquakes. In the high-Q_P and high-Q_S patch in the Futagawa segment, the large-slip area of the mainshock (surrounded by the red dashed line in Fig. 6) estimated by Asano and Iwata (2016) is located.

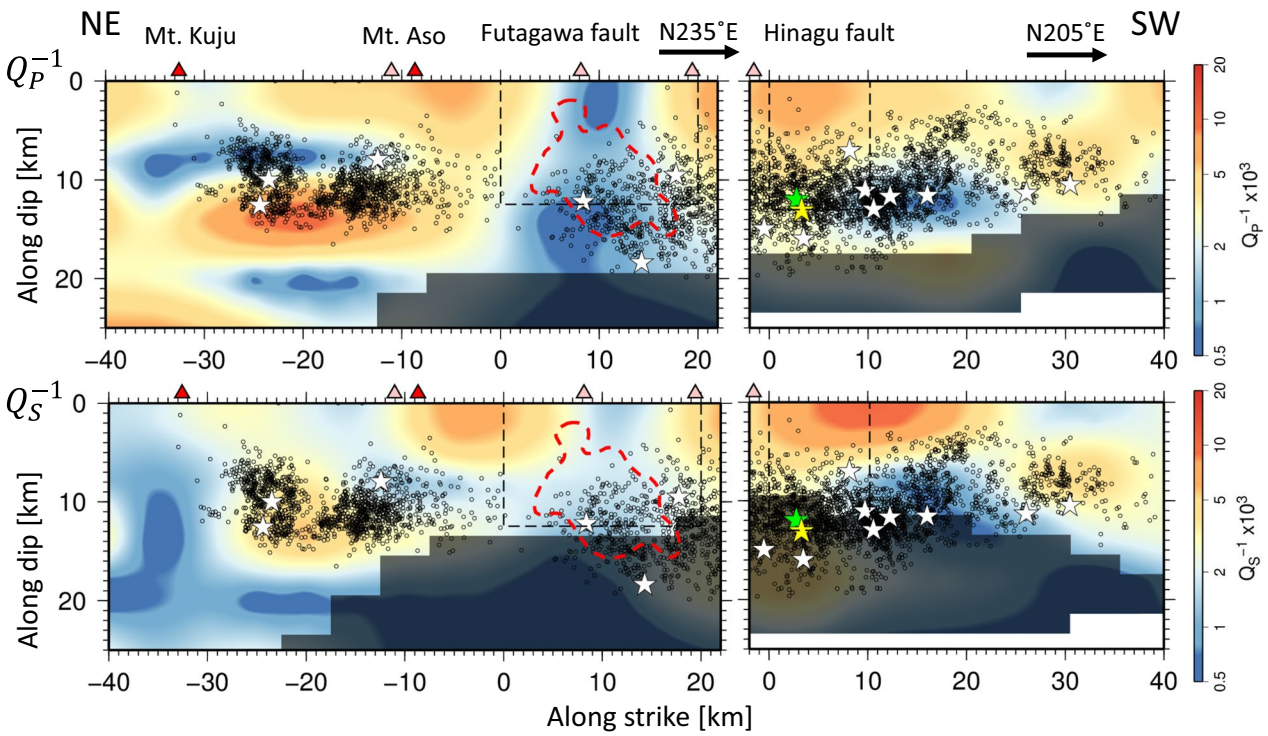

Fig. 6 Q_P^{-1} (*upper*) and Q_S^{-1} (*lower*) distribution along the planes shown in Fig. 5. Two *dashed squares* indicate the source fault planes estimated by Kato et al. (2016) and GSI (2016). The region enclosed by the *red dashed line* is the large-slip area (≥3.0 m) of the mainshock estimated by Asano and Iwata (2016). See the captions of Figs. 3 and 5 for an explanation of the symbols

Such a large-slip area located in a high-Q zone is seen for other large earthquakes (e.g., Liu et al. (2014) for the 2011 Tohoku earthquake; Rietbrock (2001) for the 1995 Kobe earthquake). The high-Q_P and high-Q_S zone might be attributed to the strongly coupled area along the Futagawa fault segment. The aftershock activity in the high-Q_P and high-Q_S zone vanishes beneath the southwest side of Mt. Aso. This is near the boundary between the high-Q_P zone and the volcanic low-Q_P zone. Yagi et al. (2016) estimated the source rupture process of the mainshock using teleseismic records and showed that the northeast edge of the large-slip area is located in this region, suggesting that the high-temperature area around the magma chamber of Mt. Aso contributes to the termination of the rupture during the mainshock. The low-Q_P region beneath Mt. Aso may give new evidence for this suggestion.

Conclusions

We estimated the 3-D Q_P and Q_S structures around the source region of the 2016 Kumamoto earthquakes. In the volcanic region, low-Q_P and low-Q_S patches were located around active volcanoes. Many of aftershocks occurred between the high- and low-Q_P patches beneath the area from Mt. Kuju to Mt. Aso, and beneath Mt. Yufu-dake, aftershocks locally took place in a low-Q_P and low-Q_S zone. In the source region, two high-Q_P and high-Q_S zones exist along the Futagawa and the Hinagu fault segments in the upper crust, and numerous aftershocks occurred in these zones, while in the lower crust, a low-Q_P zone exists entirely below the source region, which might be caused by the presence of fluids from the mantle. The large-slip area of the mainshock inferred from a source inversion is located in the high-Q_P and high-Q_S zone of the Futagawa fault segment in the upper crust. The eastern edge of this zone adjoins a low-Q_P zone beneath Mt. Aso. This suggests that the high-temperature area around the magma chamber might have contributed to the termination of the rupture of the mainshock.

Additional file

Additional file 1. Additional descriptions of corner frequency estimation and "resolvability". **Figure S1.** Example of estimation of the corner frequency. *Black line* indicates the observed spectral ratio. *Blue solid* and *dashed lines* denote the average of all the spectral ratios and its standard deviation, respectively. The *red line* indicates the fitted curve of Eq. (S1). **Figure S2.** Examples of spectral fitting to evaluate t^*. *Light green* and *blue intervals* indicate time windows for a signal and noise, respectively. *Green*

and *blue lines* denote the Fourier amplitude spectra for signal and noise, respectively. The *red line* indicates the spectrum of the signal divided by the source spectrum, and the *black dashed line* denotes the regression line, which is given in Eq. (3) in the main text. **Figure S3.** Results of the CRTs for **a** Q_P^{-1} and **b** Q_S^{-1}. The *green lines* indicate the location of R=0.75. **Figure S4.** Results of the RRTs for **a** Q_P^{-1} and **b** Q_S^{-1}. The *left-* and *right-hand panels* show the input and output structures, respectively. **Figure S5.** Lateral distribution of the estimated Q_P^{-1} and Q_S^{-1} in **a** the upper and **b** lower crust. The region *shaded by gray* shows low resolution, where the resolvability R of the CRTs is smaller than 0.75. *Green*, *yellow*, and *sky blue stars* indicate the epicenters of the largest foreshock (M_{JMA}6.5), the mainshock (M_{JMA}7.3), and the induced event (M_{JMA}5.7), respectively. *White stars* show events of magnitude larger than M_{JMA}5.0 for one month following the largest foreshock. *Black circles* indicate the epicenters with $2.0 \leq M_{JMA} < 5.0$ occurring for one month following the foreshock. Active and quaternary volcanoes are shown as *red* and *peach triangles*, respectively. *Purple lines* denote active faults (Nakata and Imaizumi 2002). *Black lines* are contours of altitude with intervals of 300 m. **Figure S6.** Lateral distribution of estimated Q_P/Q_S in the crust. See the caption of Figure S5 for other explanations.

Abbreviations

CRTs: checkerboard resolution tests; GSI: Geospatial Information Authority of Japan; Hi-net: High Sensitivity Seismograph Network Japan; JMA: Japan Meteorological Agency; NIED: National Research Institute for Earth and Disaster Resilience; PHS: Philippine Sea; RRTs: restoring resolution tests.

Authors' contributions

MK carried out the analysis. HT and HO participated in the study design. MK and HT drafted this manuscript. All authors read and approved the final manuscript.

Acknowledgements

We are grateful to the editor, Dr. Stephen Bannister, and the three reviewers, Dr. Thomas Hearn and two anonymous reviewers, who provided us with constructive comments and suggestions that have improved this paper. We used the Hi-net velocity waveform data in the NIED and the source location from JMA-Unified Hypocenter Catalogs. We also used a computer program by Zhao et al. (1992, 1994) for the ray tracing. We used the elevation data by GSI 50 m mesh heights and GMT software (Wessel and Smith 1998). This study is partially supported by KAKENHI (26282105).

Competing interests

The authors declare that they have no competing interests.

Publisher's Note

Received: 30 December 2016 Accepted: 14 July 2017
Published online: 26 July 2017

References

Aizawa K, Asaue H, Koike K, Takakura S, Utsugi M, Inoue H, Yoshimura R, Yamazaki K, Komatsu S, Uyeshima M, Koyama T, Kanda W, Shiotani T, Matsushima N, Hata M, Yoshinaga T, Uchida K, Tsushima Y, Shito A, Fujita S, Wakabayashi A, Tsukamoto K, Matsushima T, Miyazaki M, Kondo K, Takashima K, Hashimoto T, Tamura M, Matsumoto S, Yamashita Y, Nakamoto M, Shimizu H (2017) Seismicity controlled by resistivity structure: the 2016 Kumamoto earthquakes, Kyushu Island, Japan. Earth Planets Space 69:4. doi:10.1186/s40623-016-0590-2

Aki K, Chouet B (1975) Origin of coda waves: source, attenuation, and scattering effects. J Geophys Res 80:3322–3342. doi:10.1029/JB080i023p03322

Anderson DL, Ben-Menahem A, Archambeau CB (1965) Attenuation of seismic energy in the upper mantle. J Geophys Res 70:1441–1448. doi:10.1029/JZ070i006p01441

Asano K, Iwata T (2016) Source rupture processes of the foreshock and mainshock in the 2016 Kumamoto earthquake sequence estimated from the kinematic waveform inversion of strong motion data. Earth Planets Space 68:147. doi:10.1186/s40623-016-0519-9

Cho I, Kuwahara Y (2013) Constraints on the three-dimensional thermal structure of the lower crust in the Japanese Islands. Earth Planets Space 65:855–861. doi:10.5047/eps.2013.01.005

Eberhart-Phillips D, Chadwick M (2002) Three-dimensional attenuation model of the shallow Hikurangi subduction zone in the Raukumara Peninsula, New Zealand. J Geophys Res 107:ESE3-1–ESE3-15. doi:10.1029/2000JB000046

Geospatial Information Authority of Japan (2016) Fault model of the 2016 Kumamoto earthquakes (preliminary version). http://www.gsi.go.jp/common/000140781.pdf **(in Japanese)**. Accessed 24 July 2016

Horiguchi K, Matsuda J (2013) Geographical distribution of ^{3}He/^{4}He ratios in north Kyushu, Japan: geophysical implications for the occurrence of mantle-derived fluids at deep crustal levels. Chem Geol 340:13–20. doi:10.1016/j.chemgeo.2012.12.008

Karato S (2003) Mapping water content in the upper mantle, inside the subduction factory. Geophys Monogr Ser 138:135–152. doi:10.1029/138GM08

Kato A, Nakamura K, Hiyama Y (2016) The 2016 Kumamoto earthquake sequence. Proc Jpn Acad Ser B 92:358–371. doi:10.2183/pjab.92.359

Kita S, Nakajima J, Hasegawa A, Okada T, Katsumata K, Asano Y, Kimura T (2014) Detailed seismic attenuation structure beneath Hokkaido, northeastern Japan: arc-arc collision process, arc magmatism, and seismotectonics. J Geophys Res 119:6486–6511. doi:10.1002/2014JB011099

Ko Y, Kuo B, Hung S (2012) Robust determination of earthquake source parameters and mantle attenuation. J Geophys Res 117:B04304. doi:10.1029/2011JB008759

Komatsu M, Oda H (2015) Three-dimensional P-wave attenuation structure beneath Southwest Japan. Zisin 2(67):105–124. doi:10.4294/zisin.67.105 **(in Japanese with English abstract)**

Lawson CL, Hanson RJ (1974) Solving least squares problems. Prentice-Hall Inc, Upper Saddle River

Liu X, Zhao D (2014) Structural control on the nucleation of megathrust earthquakes in the Nankai subduction zone. Geophys Res Lett 41:8288–8293. doi:10.1002/2014GL062002

Liu X, Zhao D (2015) Seismic attenuation tomography of the Southwest Japan arc: new insight into subduction dynamics. Geophys J Int 201:135–156. doi:10.1093/gji/ggv007

Liu X, Zhao D, Li S (2014) Seismic attenuation tomography of the Northeast Japan arc: insight into the 2011 Tohoku earthquake (Mw 9.0) and subduction dynamics. J Geophys Res 119:1094–1118. doi:10.1002/2013JB010591

Mamada Y, Takenaka H (2004) Strong attenuation of shear waves in the focal region of the 1997 Northwestern Kagoshima earthquakes, Japan. Bull Seism Soc Am 94:464–478. doi:10.1785/0120030032

Matsumoto S, Nakao S, Ohkura T, Miyazaki M, Shimizu H, Abe Y, Inoue H, Nakamoto M, Yoshikawa S, Yamashita Y (2015) Spatial heterogeneities in tectonic stress in Kyushu, Japan and their relation to a major shear zone. Earth Planets Space 67:172. doi:10.1186/s40623-015-0342-8

Matsumoto S, Nishimura T, Ohkura T (2016) Inelastic strain rate in the seismogenic layer of Kyushu Island, Japan. Earth Planets Space 68:207. doi:10.1186/s40623-016-0584-0

Modiano T, Hatzfeld D (1982) Experimental study of the spectral content for shallow earthquakes. Bull Seism Soc Am 72:1739–1758

Nakata T, Imaizumi T (eds) (2002) Digital active fault map of Japan. University of Tokyo Press, Tokyo

Okada Y, Kasahara K, Hori S, Obara K, Sekiguchi S, Fujiwara H, Yamamoto A (2004) Recent progress of seismic observation networks in Japan—Hi-net, F-net, K-NET and KiK-net. Earth Planets Space 56:xv–xxviii. doi:10.1186/BF03353076

Pozgay SH, Wiens DA, Conder JA, Shiobara H, Sugioka H (2009) Seismic attenuation tomography of the Mariana subduction system: implications for thermal structure, volatile distribution, and slow spreading dynamics. Geochem Geophys Geosyst 10:Q04X05. doi:10.1029/2008GC002313

Rautian TG, Khalturin VI, Martynov VG, Molnar P (1978) Preliminary analysis of the spectral content of P and S waves from local earthquakes in the Garm, Tadjikistan region. Bull Seism Soc Am 68:949–971

Rietbrock A (2001) P wave attenuation structure in the fault area of the 1995 Kobe earthquake. J Geophys Res 106:4141–4154. doi:10.1029/2000JB900234

Saiga A, Matsumoto S, Uehira K, Matsushima T, Shimizu H (2010) Velocity structure in the crust beneath the Kyushu area. Earth Planets Space 62:449–462. doi:10.5047/eps.2010.02.003

Saita H, Nakajima J, Shiina T, Kimura J (2015) Slab-derived fluids, forearc dehydration, and sub-arc magmatism beneath Kyushu, Japan. Geophys Res Lett 42:1685–1693. doi:10.1002/2015GL063084

Scherbaum F (1990) Combined inversion for the three-dimensional Q structure and source parameters using microearthquake Spectra. J Geophys Res 95:12423–12438. doi:10.1029/JB095iB08p12423

Somei K, Asano K, Iwata T, Miyakoshi K (2014) Source scaling of inland crustal earthquake sequences in Japan using the S-wave coda spectral ratio method. Pure Appl Geophys 171:2747–2766. doi:10.1007/s00024-014-0774-2

Thurber CH (1983) Earthquake locations and three-dimensional crustal structure in the Coyote Lake Area, central California. J Geophys Res 88:8226–8236. doi:10.1029/JB088iB10p08226

Ueno H, Hatakeyama S, Aketagawa T, Funasaki J, Hamada N (2002) Improvement of hypocenter determination procedures in the Japan Meteorological Agency. Quater J Seismol 65:123–134 **(in Japanese with English abstract)**

Wang Z, Zhao D, Liu X, Li X (2017) Seismic attenuation tomography of the source zone of the 2016 Kumamoto earthquake (*M* 7.3). J Geophys Res 122:2988–3007. doi:10.1002/2016JB013704

Wessel P, Smith WHF (1998) New, improved version of the generic mapping tools released. EOS Trans Am Geophys Union 79:579

Yagi Y, Okuwaki R, Enescu B, Kasahara A, Miyakawa A, Otsubo M (2016) Rupture process of the 2016 Kumamoto earthquake in relation to the thermal structure around Aso volcano. Earth Planets Space 68:118. doi:10.1186/s40623-016-0492-3

Yoshida S (2016) Earthquake in Oita triggered by the 2016 *M*7.3 Kumamoto earthquake. Earth Planets Space 68:176. doi:10.1186/s40623-016-0552-8

Zelt CA (1998) Lateral velocity resolution from three-dimensional seismic refraction data. Geophys J Int 135:1101–1112. doi:10.1046/j.1365-246X.1998.00695.x

Zhao D, Hasegawa A, Horiuchi S (1992) Tomographic imaging of P and S wave velocity structure beneath northeastern Japan. J Geophys Res 97:19909–19928. doi:10.1029/92JB00603

Zhao D, Hasegawa A, Kanamori H (1994) Deep structure of Japan subduction zone as derived from local, regional and teleseismic events. J Geophys Res 99:22313–22329. doi:10.1029/94JB01149